CrossMark

Structure, electrical and magnetic properties of $La_{0.67}Ca_{0.33-x}K_xMnO_3$ polycrystalline ceramic

Di Li[1] · Qingming Chen[1] · Zhiyu Li[1] · Hui Zhang[1] · Yalin Zhang[1]

Abstract A systematic investigation of structure, electrical and magnetic properties of polycrystalline ceramics $La_{0.67}Ca_{0.33-x}K_xMnO_3$ ($x = 0.05, 0.10, 0.15, 0.20, 0.25$) samples, prepared by sol–gel method had been undertaken. As K content increases the crystal structures were transformed from orthorhombic to rhombohedral structure identified by X-ray diffraction, and the effect of increasing K ion is to increment the Mn–O–Mn bond angle. The surface morphology was investigated by scanning electron microscope, which indicates that grain size decreasing with increasing of K^+. Temperature dependence of resistivity ($\rho - T$) was measured by standard four-probe method. The insulator–metal transition temperature (T_P) shifted to higher temperature and the temperature coefficient of resistivity decreased sharply with the substitution K^+ for Ca^{2+} ion. The temperature dependence of magnetization (M–T) shown that Curie temperature (T_C) was increasing with the increase of K content, which can be explained by enhancement of double–exchange interaction. The data of resistivity on low-temperature ($T < T_P$) had been fitted with the relation $\rho(T) = \rho_0 + \rho_2 T^2 + \rho_{4.5} T^{4.5}$; the high-temperature ($T > T_P$) resistivity data were explained using small-polaron hopping and variable-range hopping models. Resistivity data in whole temperature range (100–320 K) could be fitted by percolation model. Polaron activation energy E_a was found to decrease with the content K^+ increasing, which suggested that K doping increase bond angle Mn–O–Mn, thereby the effective band gap was decreased and the double exchange coupling was increased of, this is the reason for the decrease of resistivity.

1 Introduction

The unique properties such as colossal magnetoresistance (CMR) and metal–insulator transition of perovskite-based manganite as $La_{1-x}A_xMnO_3$ (A is the divalent or monovalent metal ion) had been extensively studied [1, 2]. Various magnetic phases, Jahn–Teller effect and charge ordering are also some of interesting phenomena which is showed in these perovskite manganites. The research efforts in the CMR materials area have been focused on the optimization of doped compounds with the aim to enhancing and tuning their physical properties [3, 4]. However, there is no satisfactory model accounting for the associated phenomenon that has been referred to as colossal magnetoresistance and electrical transport [5].

Undoped $LaMnO_3$ is an A-type antiferromagnetic insulator. When divalent cation (such as Ca^{2+} and Sr^{2+}) substitutes for La^{3+}, doped-$LaMnO_3$ can be driven into a metallic and ferromagnetic state. Zener proposed that the spin structure and the electronic properties of perovskite manganite were correlated via the double–exchange (DE) mechanism, which can provide a qualitative explanation [6]. Both Mn^{3+} and Mn^{4+} ions possess local spin ($S = 3/2$) from their lower t_{2g} orbitals, and Mn^{3+} has an extra electron in the e_g orbital, which is responsible for. The spin of $e1$ g electron in Mn^{3+} is ferromagnetically coupled to the local spin of $t3$ 2g according to Hund's rule. Except for the hole carrier density controlled by the Mn^{3+}/Mn^{4+} ratio, the oxygen vacancies, the tolerance factor (t), the mean A-site cation radius $<r_A>$ and the size mismatch σ^2 have also been exhibited influence the double exchange [7,

✉ Hui Zhang
harry_zhang71@163.com

1 Faculty of Materials Science and Engineering, Kunming University of Science and Technology, Kunming 650093, People's Republic of China

8]. However, Millise et al. [9] argued that the physics of manganite is controlled by the interaction between large Hund coupling effect and strong electron–phonon coupling that optimizes the electronic activation energy by the generation of a ferromagnetic phase.

Electrical conductivity of divalent substituted La perovskites have been researched in much detail, compared to those monovalent doped systems. Because the valance state of the alkali metal ions is $+1$, La substitution of alkali metals effect the ratio of Mn^{3+} and Mn^{4+} ions. So this influences the DE interaction. In addition, preparation method can also greatly affect the electrical and magnetic property due to the influence of surface morphology, microstructure, chemical homogeneity and particle size of the ceramic samples [10, 11]. In order to obtain homogenous composition in the compound, the higher temperature, longer sintering time and several times of intermediate grinding and sinter are necessary in the conventional solid state reaction. Spray-drying is another method to synthesize the polycrystalline ceramic samples. In this method, a solution of particular concentration and a co-current flow atomization system are necessary. So this method increasing the difficulty of the sample preparation and preparation cost. In co-precipitation method, the pH value of solution need to be controlled, and the aging of solution need a long time. Reddy et al. synthesized conducting nanocomposite by in situ chemical oxidative polymerization and other method, there were a good method to synthetic similar materials [12–20].

S–G method has attracted great interest in recent years by the reason for its unique strengths [21, 22]. In this paper, a methanol and deionized water solvent sol–gel (S–G) routine has been used to fabricate high purity and homogeneity samples. This improved S–G process can not only keep the advantages of water solvent S–G technique but also greatly shorten the experimental period to tens of minutes. In present work, we systemically study the electrical transport properties of $La_{0.67}Ca_{0.33-x}K_xMnO_3$ ($x = 0.05, 0.1, 0.15, 0.20, 0.25$), hoping to obtain further physical interpretation for the properties. The electrical resistivity experimental data both in the high temperature and low temperature phases have been analyzed with different theoretical models [23, 24].

2 Experiments

A series of polycrystalline ceramics $La_{0.67}Ca_{0.33-x}K_xMn_3$ ($x = 0.05$–0.25) were prepared by sol–gel technique. Firstly, stoichiometric amount of $KHCO_3$ had been weighted and dissolved in dilute nitric acid to transform it into nitrate. And then dissolving the precursors with high purity ($La(NO_3)_3 \cdot nH_2O$, $Ca(NO_3)_2$, $Mn(NO_3)_2 \cdot 4H_2O$) in mixed solution consisting of methyl alcohol and deionized water. The citric acid as chelating agent with molar ratio to metal ions as 4:1 and the ethylene–glycol as gelification agent were added to the mixed solution. The step made at room temperature until reaching total dissolution. The solution was completely stirred and evaporated on magnetic stirrer at 88 °C hot plate until formation the orange transparent gel. The xerogel was obtained after putting the gel into oven at 140 °C for 24 h. Secondly, the xerogel was ground into power and calcined in the air at 500 °C for 8 h. Finally, the resulting calcined powder was ground again and pressed into pellet, than sintered at 1250 °C for 12 h to obtain bulk polycrystalline ceramics target. All raw materials bought from *Sinopharm Chemical Reagent Company, China*, and the weight of raw material was shown in Table 1.

Phase purity and the lattice parameter refining of the samples were checked through X-ray powder diffract meter using Cu Kα radiation at room temperature. The surface morphology and microstructure of the sampled were characterized by scanning electron microscope (SEM). The resistivity of the samples was measured by the standard four-probe method within the temperature range of 100–320 K. Magnetization measurements were carried out using a Quantum Design Squid MPMS magnetometer in the range of 50–320 K.

Table 1 The amount (grams) of all raw materials

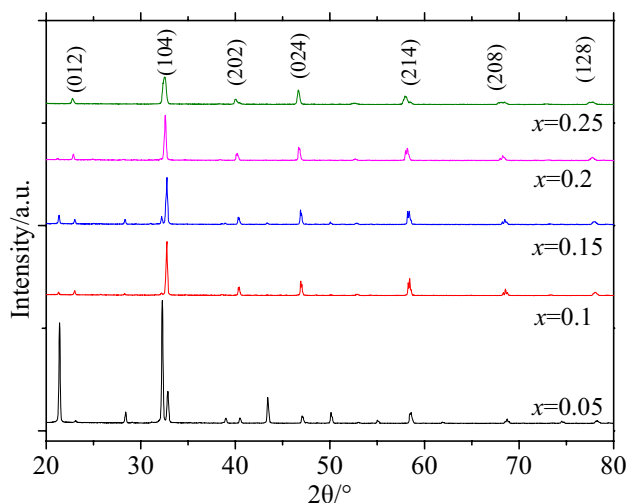| Sample name	$La(NO_3)_3 \cdot nH_2O$ (AR)	$Ca(NO_3)_2 \cdot 4H_2O$ (AR)	$Mn(NO_3)_2 \cdot 4H_2O$ ($\geq 96.5\%$)	$C_6H_6O_7 \cdot 4H_2O$ (AR)	$KHCO_3$ (AR)
$La_{0.67}Ca_{0.28}K_{0.05}MnO_3$	3.7559	0.9483	3.7402	12.0550	0.0718
$La_{0.67}Ca_{0.23}K_{0.1}MnO_3$	3.7568	0.7791	3.7410	12.0578	0.1436
$La_{0.67}Ca_{0.18}K_{0.15}MnO_3$	3.7577	0.6099	3.7419	12.0607	0.2155
$La_{0.67}Ca_{0.13}K_{0.2}MnO_3$	3.7586	0.4406	3.7428	12.0635	0.2874
$La_{0.67}Ca_{0.08}K_{0.25}MnO_3$	3.7594	0.2712	3.7437	12.0663	0.3593

Fig. 1 XRD diffraction patterns of $La_{0.67}Ca_{0.33-x}K_xMnO_3$ ($x=0.05$, 0.1, 0.15, 0.2 and 0.25)

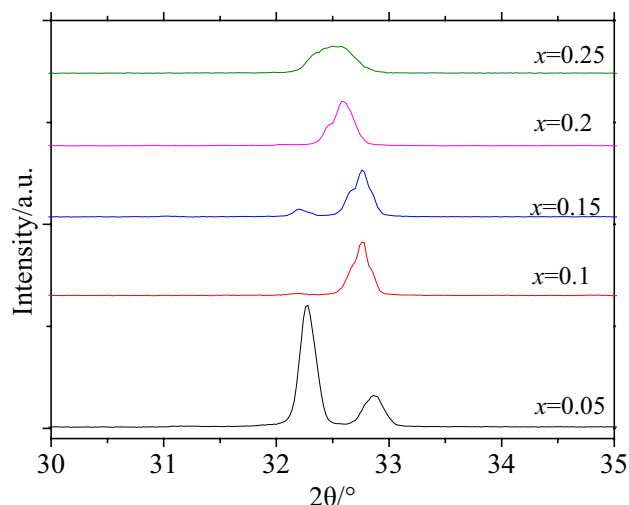**Fig. 2** Enlarged view of the strongest diffraction peak of $La_{0.67}Ca_{0.33-x}K_xMnO_3$ ($x=0.05$, 0.10, 0.15, 0.20, 0.25)

3 Results and discussion

3.1 Structures and surface morphology of the LCKMO samples

Synthesized samples of the pristine $La_{0.67}Ca_{0.33-x}K_xMnO_3$ ($x=0.05$, 0.10, 0.15, 0.20, 0.25) composites have been analyzed for the phase formation by XRD as shown in Fig. 1. It indicates that all the samples crystallize in single-phase with no measurable impurity phases. The intensity of $x=0.05$ is higher than other samples which may be due to the preferred orientation presence in this sample. The intensity of almost all of the diffraction peaks in Fig. 1 decreases with increased K content, meanwhile the FWHM turns broader, which clearly indicate that the crystalline quality of LCMO ceramics turns worse when K is introduced in. The refined values of the lattice constant are given in Table 2. It is clear that the substitutional variation of K^+ causes significant structural changes. It can be indexed that the samples of $x=0.05$ and 0.1 shown an orthorhombic perovskite structure whit *Pnma* space group, whereas, when $x=0.15$, 0.20, 0.25, the structure of samples transformed into rhombohedral lattice (hexagonal setting) with $R\bar{3}c$ space group which is consistent with the previously reported results [25, 26].

And the band angle of Mn^{3+}–O^{2-}–Mn^{4+} has been increasing with the increase K^+.

The enlarged view of the strongest diffraction pack of $La_{0.67}Ca_{0.33-x}K_xMnO_3$ ($x=0.05$, 0.10, 0.15, 0.20, 0.25) is displayed in Fig. 2. It is worth noticing that the strongest diffraction peak shifts to lower degree with increasing K content, which indicates that the increase of K^+ substitution increases the volume of the unit cell. It can be also seen from Table 2 that the cell volumes obtained from Cell Refinement tend to increase with increasing K content. It is mainly due to the fact that the K^+ ion (ionic radius = 1.55 Å) is partially substituted the smaller Ca^{2+} (ionic radius = 1.18 Å), which makes the cell volume increase. The diffraction peaks broadening with the increasing of K^+, which indicates the grain size has decreased. It can be seen from the SEM images that grain size decreasing with the increasing of K^+.

The surface morphology of the polycrystalline ceramic $La_{0.67}Ca_{0.33-x}K_xMnO_3$ ($x=0.10$, 0.20, 0.25) studied by SEM is presented in Fig. 3(a–c). It is shown that grain size decreasing with increasing of K^+. And it also clearly shows that few pores or holes are observed. The reason for this phenomenon is that the grain boundaries and other internal defects of the ceramic samples are less, which essentially reflects the intrinsic behavior of the electric properties [27].

Table 2 The lattice parameters of $La_{0.67}Ca_{0.33-x}K_xMnO_3$

x (K content)	a (Å)	b (Å)	c (Å)	V (Å)³	Mn–O–Mn (°)	Structure
0.05	5.4493	7.7197	5.4738	230.27	165.269	Orthorhombic
0.10	5.4846	7.8008	5.4658	233.85	165.419	Orthorhombic
0.15	5.4885	5.4885	13.3706	348.81	166.554	Rhombohedral
0.20	5.5046	5.5046	13.4295	352.41	166.561	Rhombohedral
0.25	5.5275	5.5275	13.3902	354.30	166.530	Rhombohedral

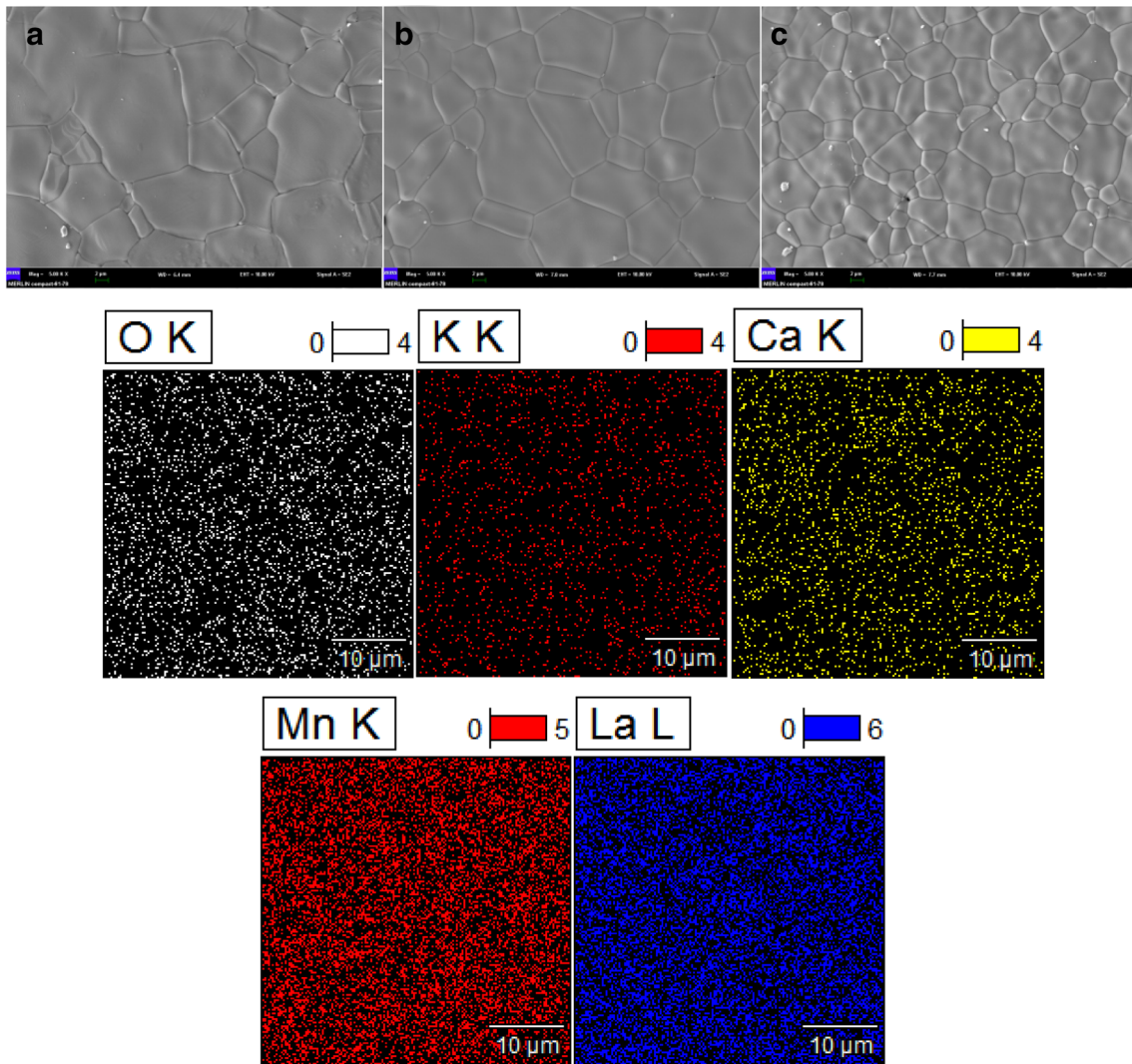**Fig. 3** SEM images of $La_{0.67}Ca_{0.33-x}K_xMnO_3$ **a** $x=0.1$ **b** $x=0.2$ and **c** $x=0.25$ and elemental mapping images of $La_{0.67}Ca_{0.05}K_{0.25}MnO_3$

In present system, the very few pores have very little effect on the resistivity, therefore it can be deduced that K^+ content may be a major part in determining the electrical property. The elemental mapping images of $La_{0.67}Ca_{0.05}K_{0.25}MnO_3$ shown in Fig. 3, which indicated all elements (La, Ca, K, Mn, O) were evenly distributed on the grain surface.

3.2 Electrical Properties of the LCKMO samples

In previous work, some conducting materials such as nanocomposite had been investigated on the conductivity [28–30]. In this paper, we focus on the resistivity to explain the electrical transport behavior of the samples. Temperature dependence of resistivity of the polycrystalline ceramic $La_{0.67}Ca_{0.33-x}K_xMnO_3$ is shown in Fig. 4, which was measured in warming-up processes. It can be seen that the samples for $x=0.05, 0.1, 0.15, 0.20, 0.25$ show metal–insulator
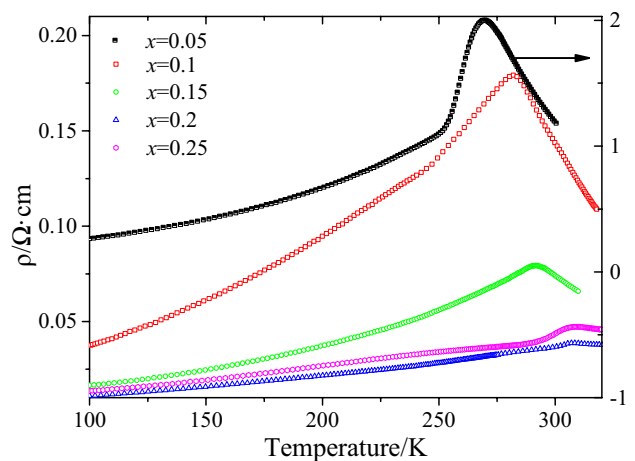

Fig. 4 Temperature dependence of resistivity of the $La_{0.67}Ca_{0.33-x}K_xMnO_3$ ceramic samples

Table 3 Experimental date of $La_{0.67}Ca_{0.33-x}K_xMnO_3$ ceramic samples

x	$<r_A>$ (Å)	T_P (K)	TCR_{max} (% K^{-1})	ρ_{max} (Ω cm)
0.05	1.222	269.7	5.44	2.000
0.10	1.241	282.1	1.11	0.179
0.15	1.259	291.5	2.47	0.079
0.20	1.278	307.1	1.68	0.039
0.25	1.296	308.9	1.57	0.047

transition at T_P. It can also be observed from Fig. 4 and Table 3 that the T_P shifts to higher temperature and resistivity decreases constantly with increasing K content. It can be seen from Table 2 that the increasing K ion is to increment the Mn–O–Mn bond angle when $x = 0.05–0.20$, the mismatch effect would demote the localization of e_g electrons thereby increasing the double exchange effect which results in the increase of conductivity and in turn the observed shift in T_P [31]. But when $x = 0.25$ the resistivity is increased compared with $x = 0.2$, it is due to the Mn–O–Mn bond angle has been decrease as show in Table 2, furthermore, as the doping of K^+ increases, the Mn^{4+} concentration exceeds that of Mn^{3+}, thereby, $Mn^{3+}–O–Mn^{4+}$ pairs becomes fewer. This favors $Mn^{4+}–O–Mn^{4+}$ super exchange interaction and weakens the DE interaction [24]. From Fig. 5, it can be seen that temperature coefficient of resistivity (TCR) sharply decreases when the content of K exceeds 0.05 which is due to the metal–insulator transition peak becomes borderer with the increasing of K^+ [32].

Different conduction mechanisms of resistivity have been reported at different temperature ranges. There are three temperature regimes considered in this paper, viz. metallic
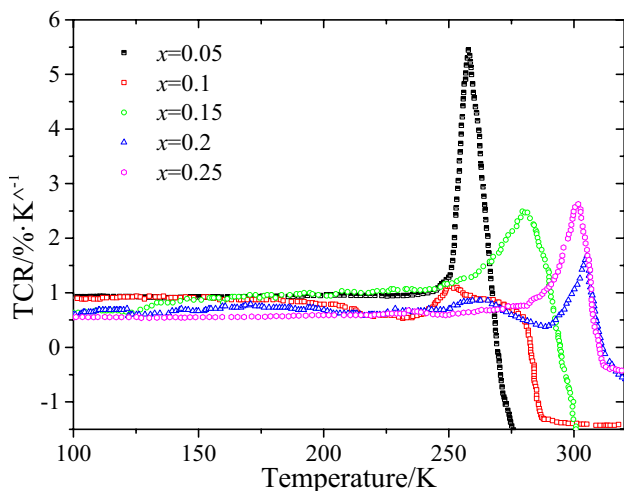

Fig. 5 Temperature coefficient of resistivity for $La_{0.67}Ca_{0.33-x}K_xMnO_3$ ceramic samples

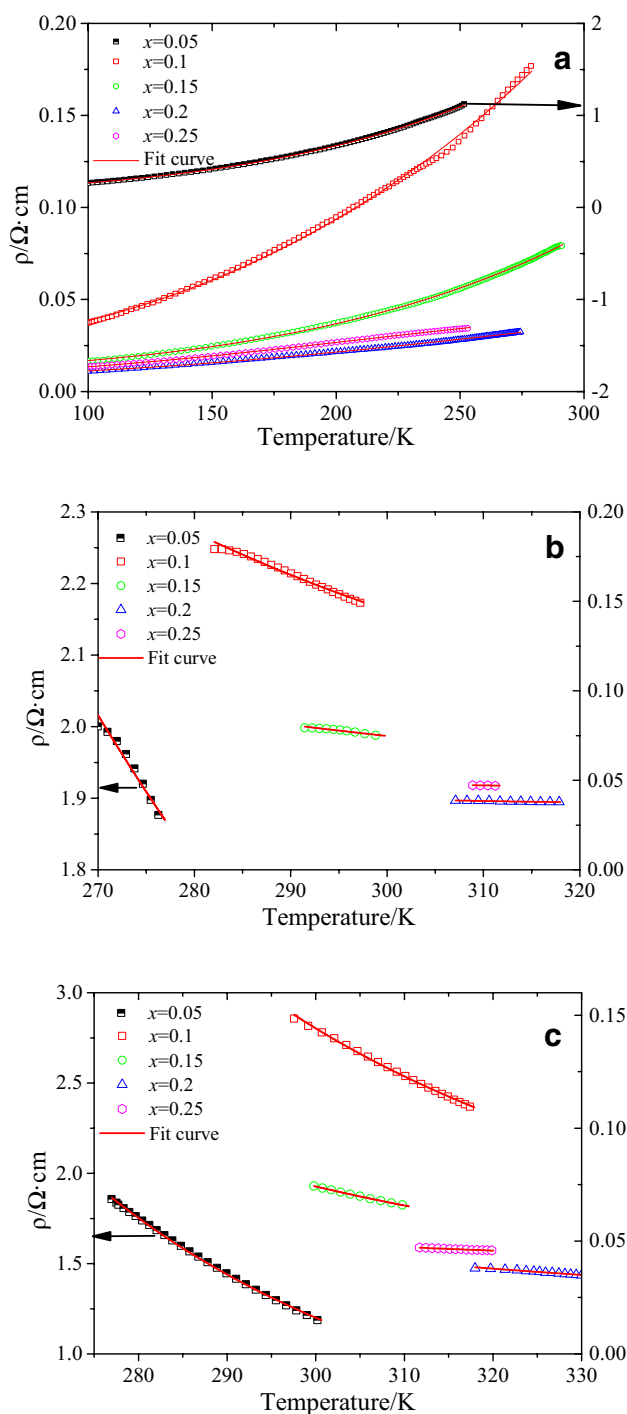

Fig. 6 Fit curve of electrical resistivity in different temperature range **a** $T < T_P$; **b** $T_P < T < \theta_D/2$ l; **c** $T > \theta_D/2$

regime ($T < T_P$), insulating regime ($T > \theta_D/2$, θ_D is Debye's temperature) and competing regime ($T_P < T < \theta_D/2$).

3.2.1 Low temperature range (T < T_P)

Figure 6a show that at the low temperature (T < T_P), the temperature dependent resistivity exhibits metallic behavior for all samples. In order to investigate the transport mechanism in metallic region, Eq. (1) is a well-known empirical equation has been used to fit with the experimental data: [33, 34].

$$\rho_{FM}(T) = \rho_0 + \rho_2 T^2 + \rho_{4.5} T^{4.5} \tag{1}$$

where ρ_0 is the residual resistivity, it's arising from grain boundary scattering and other temperature independent mechanisms. $\rho_2 T^2$ may be due to the electron–electron scattering process which is generally observed in manganites. The $\rho_{4.5} T^{4.5}$ is attributed to electron–electron, electron–magnon and electron–phonon scattering process in the ferromagnetic region. The quality of these fittings is evaluated by comparing the square of liner correlation coefficient R^2 [35]. The fitting graphs and related data of the experimental with Eq. (1) are showing in Fig. 6a and Table 4, respectively. From the fitting results it is shown that the R^2 for both samples are closed to 1. It can be seen the ρ_0 decrease ($x = 0.05$–0.20) with the increasing of K^+ from Table 4, which indicate that K^+ doping increasing grain boundary (show in Fig. 3) but it also decreases the grain boundary scattering and increases Mn–O–Mn bond angle (show in Table 2), this is the cause of resistivity decreases with the grain boundary increasing which is contradicted with common sense. It is notable that when $x = 0.20$ and 0.25 the $\rho_{4.5}$ turned out to be negative, which is may be due to at high doping content of K^+, the electron–magnon and electron–phonon scattering process are conducive to conductivity or it have been changed to anther scattering process.

Table 4 Low temperature fitting parameters obtained from fitting experimental data with Eq. (1) (T < T_P)

x	ρ_0 (Ω cm × 10^{-3})	ρ_2 [(Ω cm K^{-1}) × 10^{-7}]	$\rho_{4.5}$ [(Ω cm K^{-1}) × 10^{-13}]	R^2
0.05	166.54	95.76	53.47	0.9999
0.10	21.46	16.81	2.15	0.9986
0.15	11.35	5.30	1.90	0.9998
0.20	7.62	3.63	− 3.02	0.9997
0.25	8.43	5.15	− 1.04	0.9991

In addition, the electron–electron scattering term $\rho_2 T^2$ in Eq. (1) is larger than that of electron–magnon (phonon) $\rho_{4.5} T^{4.5}$ for all samples. Therefore, the electron–electron scattering displays a major role in the conductivity of samples in the metallic regime.

3.2.2 High temperature range (T > θ_D/2)

The small-polaron hopping mole (SPH) is used to explain the temperature dependent resistivity at high temperature range (T > θ_D/2). The polaron hopping mole could be either adiabatic Eq. (2) or non-adiabatic Eq. (3) approximations.

$$\rho_{PM}(T) = \rho_{os} T \exp(Ea / k_B T) \text{ (adiabatic)} \tag{2}$$

$$\rho_{PM}(T) = \rho_{os} T^{1.5} \exp(Ea / k_B T) \text{ (non-adiabatic)} \tag{3}$$

where ρ_{os} is resistivity coefficient, E_a is the polaron activation energy and k_B is the Boltzmann constant. According to find the type of hopping, the Holstein's relation has been used [36]. From this relation, the polaron band width J and critical polaron energy band width φ should obey the following condition: $J/\varphi > 1$ for adiabatic hopping and $J/\varphi < 1$ for non-adiabatic hopping as following Eq. (4)

$$\frac{J}{\varphi} = 1.33 \left(\frac{kB\theta D}{Ea} \right)^{\frac{1}{4}} \tag{4}$$

The fitting graphs and related data of the experimental with Eq. (2) and Eq. (3) are showing in Fig. 6c and Table 5, respectively. It clearly seen from Table 5 that except of $x = 0.05$, all samples are adiabatic hopping mechanism. And E_a decreasing with the increasing of K ion, this is may be attributed to the increasing content of K ion that induces Mn–O–Mn bond angle increase. Thereby, widening the bandwidth and degrading the effective mass of the charge carrier. Due to this effect, the effective band gap decrease with increasing of K ion. Therefore, lower values of activation energize are needed for the charge carriers to overcome this band gap [37]. Furthermore, the small-phonon coupling γ_P is a measure of electron–phonon interaction in the manganite. The γ_P value of all samples are presented in Table 5, it has been suggested that electron–phonon interaction become waning with the increasing of K ion, which favors the movement of the charge carriers [38]. Millis et al. [39] did the theoretical calculation which

Table 5 SPH model fitting parameters obtained from fitting experimental data with Eqs. (2) and (3) (T > θ_D/2)

x	E_a (meV)	θ_D (K)	J (meV)	J (φ)	γ_P	R^2
0.05	174.47	553.9	27.45	0.962	7.310	0.9993
0.10	154.20	595.1	28.96	1.010	6.014	0.9982
0.15	136.08	599.6	29.88	1.071	5.267	0.9997
0.20	97.14	635.9	30.44	1.153	3.545	0.9858
0.25	55.63	623.4	29.99	1.318	2.071	0.9875

demonstrated that the γ_P is the crucial parameter controlling T_P: decreasing γ_P increases T_P.

3.2.3 Medium temperature range ($T_P < T < T_P$)

The temperature dependent resistivity on the range between T_P and $\theta_D/2$ may be explained on the basis of the variable-range hopping (VRH) mode. From this mode, resistivity follows Eq. (5):

$$\rho(T) = \rho_{os} \exp(T_0/T)^{0.25} \qquad (5)$$

where

$$T_0 = 16\alpha^3/k_B N(E_F) \qquad (6)$$

The inverse of localization length α is taken as 2.22 nm^{-1} as reported by Navasery et al. [40] and $N(E_F)$ is the density of states near the Fermi level. The fitting graphs and related data of the experimental with Eq. (5) are showing in Fig. 6b and Table 6, respectively. The $N(E_F)$ found to increase with K doping which suggested an appreciable increase in the number of charge carriers accompanied by increase of conductivity of K doping. This is supported by resistivity data. The observed high value of $N(E_F)$ validates the small polaron hopping nature of carriers in the presently investigated manganites [41].

3.2.4 Whole temperature range

The resistivity in the entire temperature range is analyzed using the phenomenological percolation model explained [42]. This model takes into account the contributions arising from the terms $\rho_{FM}(T)$ and $\rho_{PM}(T)$, and the combined equation as Eq. (7)

$$\rho(T) = \rho_{FM}(T)f + \rho_{PM}(T)(1-f) \qquad (7)$$

where f is the volume fraction of the ferromagnetic (FM) phases and $(1-f)$ is the paramagnetic (PM) phases. In present case $\rho_{FM}(T)$ and $\rho_{PM}(T)$ are obtained from Eqs. (1–3), respectively. Volume fraction of FM and PM phases satisfy the Boltzmann distribution:

$$f = \frac{1}{1 + \exp\left(\frac{U}{kBT}\right)} \qquad (8)$$

Table 6 VRH model fitting parameters obtained from fitting experimental data with Eq. (5) ($T_P < T < \theta_D/2$)

x	T_0 (K)	$N(E_F)$ (eV^{-1} cm^{-3})	R^2
0.05	5.42×10^6	3.75×10^{20}	0.9708
0.1	1.55×10^7	1.31×10^{20}	0.9879
0.15	2.28×10^6	8.92×10^{20}	0.9503
0.20	1.86×10^4	1.09×10^{23}	0.9618
0.25	4.80×10^3	4.23×10^{23}	0.9020

Table 7 Percolation model fitting parameters obtained from fitting experimental data with Eq. (7)

x	$\frac{U_0}{k_B}$ ($K\ 10^4$)	$T_{c\text{-mod}}$ (K)	R^2
0.05	1.87	263.93066	0.9997
0.10	1.86	285.42466	0.9980
0.15	2.26	293.01966	0.9999
0.20	2.22	312.07645	0.9992
0.25	2.45	301.19909	0.9999

where $U \approx -U0\left(1 - T/T_{c\text{-mod}}\right)$ is the energy difference between FM and PM states. $T_{c\text{-mod}}$ denotes the temperature in vicinity where resistivity has a maximum value. The experimental data have been fitted in the entail temperature range using Eq. (7) and results are summarized in Table 7. It is seen that the volume fraction f is equal to 1 (FM phase) well below the T_P, and slowly approaches to 0 (PM phase) with the temperature increases. The transition from FM to PM phase takes place slowly over a wide temperature range. The experimental data of resistivity confirms the validity of the percolation model in the presently system (Fig. 7).

3.3 Magnetic properties

Figure 8 display the temperature dependence of magnetization obtained in the zero field cooled (ZFC) processes. The $La_{0.67}Ca_{0.33-x}K_xMnO_3$ ($x = 0.05, 0.15, 0.25$) samples with applied magnetics field of 0.1 T, and the insert graphs is dM/dT versus temperature curve. The Curie temperature (T_C) was defined from the temperature of the peak of dM/dT. It can be seen from Fig. 8 that T_C is 265 K for $x = 0.05$, 279 K for $x = 0.15$ and 296 K for $x = 0.25$, which is agree with the previously reports on the similar compounds [43]. The increase of T_C with the K^+ increasing can be explained
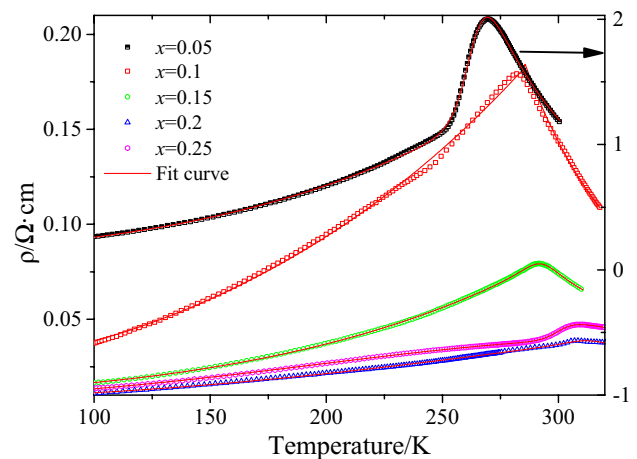

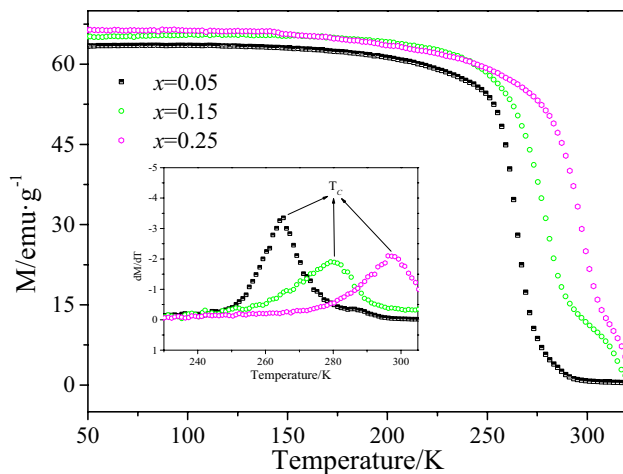**Fig. 7** Fit curve of electrical resistivity with percolation model

Fig. 8 Temperature dependence of ZFC magnetization (M) for $La_{0.67}Ca_{0.33-x}K_xMnO_3$ ($x = 0.05$, 0.15 and 0.25) samples at 0.1 T, insets show dM/dT as a function of temperature for the samples

by the enhance DE mechanism [44, 45]. From Table 2, we can see that Mn-O-Mn bond angle and the cell volume are increased induced by the larger size of K^+ substitution for Ca^{2+} and larger the A-sit radius. Thereby, the DE interaction increase and the degree of Jahn–Teller distortion is decreased, resulting in the enhancement of ferromagnetic properties and the increasing of T_C. Furthermore, the decreasing of grain size caused the T_C values increase [46].

4 Conclusion

In this paper, we had elaborated and studied the effect of the substitution of the Ca^{2+} by K^+ on the structure, morphology and electrical properties of the polycrystalline ceramic $La_{0.67}Ca_{0.33-x}K_xMnO_3$ prepared by sol–gel method. The XRD patterns confirmed this samples had been transformed from orthorhombic to rhombohedral structure. And increment the $Mn^{3+}–O^{2-}–Mn^{4+}$ bond angle with the K^+ content increasing. The substitution of Ca^{2+} for K^+ increased the volume of the unit cell. SEM images indicated that the grain sizes of these samples were decreased with the increasing of K^+. The measurement of the resistivity-temperature curves showed that the metal–insulator transition temperature T_P shifts to higher temperature, and TCR been decreases with the increasing of K^+. The low-temperature ($T < T_P$) resistivity had been relativity well fitted with the relation $\rho(T) = \rho_0 + \rho_2 T^2 + \rho_{4.5} T^{4.5}$, inducting the electron–electron scattering was the major effects in the conduction. The high-temperature ($T > T_P$) resistivity data were explained using VRH and SPH models. E_a decreased with the increasing of K ion which attributed to the Mn–O–Mn bond angle increase and effective band gap decrease, lower E_a was

needed for the charge carriers to overcome this band gap. And the γ_P value was decreased which also suggested the resistivity of samples decreases with the increasing of K ion. Percolation model had been described the resistivity on entire temperature range. The T_C increased with the increasing of K content. However, in this paper, we only provided a simple explanation of the resistivity behavior, the more deep and intrinsic understanding of electrical property needs to be researched. In the next stage, we plan to investigate the mechanism of K doping deteriorating TCR of LCMO ceramics.

References

1. A. Dhahri, F.I.H. Rhouma, S. Mnefgui, J. Dhahri, K.E. Hlil, Ceram. Int. **40**, 459 (2014)
2. A. Selmi, R. M'Nassri, W. Cheikhrouhou-Koubaa, N.C. Boudjada, A. Cheikhrouhou, Ceram. Int. **41**, 10177 (2015)
3. S. Mnefgui, N. Zaidi, N. Dhahri, J. Dhahri, E.K. Hlil, J. Magn. Magn. Mater. **384**, 219 (2015)
4. M.H. Ehsani, P. Kameli, S.F. Razavi, M.E. Ghazi, B. Aslibeiki, J. Alloys Comp. **579**, 406 (2013)
5. A.G. Gamzatov, A.B. Batdalov, L.N. Khanov, A.S. Mankevich, I.E. Korsakov, A.R. Kaul, Phys. Solid State **54**, 617 (2012)
6. C. Zener, Phys. Rev. **82**, 403 (1951)
7. D. Neila, D. Abdessalem, D. Jemai, H.E. Kebir, D. Essebti, J. Magn. Magn. Mater. **326**, 129 (2013)
8. D.G. Kuberkar, R.R. Doshia, P.S. Solankia, U. Khachara, M. Vagadiaa, A. Ravaliaa, V. Ganesanb, Appl. Surf. Sci. **258**, 9041 (2012)
9. A.J. Millis, P.B. Littlewood, B.I. Shraiman, Phys. Rev. Lett. **74**, 5144 (1995)
10. X. Yin, X. Liu, Y. Yan, Q. Chen, J. Sol-Gel. Sci. Technol. **70**, 361 (2014)
11. M. Ben Rejeba, C. Ben osmanb, Y. Regaiega, A. Marzouki-Ajmia, W. Cheikhrouhou-Koubaa, S. Ammar-Merah, A. Cheikhrouhou, T. Mhiri, J. Alloys Compd. **695**, 2597 (2017)
12. A.M. Showkat, Y.P. Zhang, S. Kim, A.I. Gopalan, K.R. Reddy, K.P. Lee, Bull. Korean Chem. Soc. **28**, 1985 (2007)
13. M. Jeem, L. Zhang, J. Ishioka, T. Shibayama, T. Iwasaki, T. Kato, S. Watanabe, Nano Lett. **17**, 3 (2017)
14. R.K. Raghava, S.B. Cheol, C.H. Yoo, P. Wonjung, R.K. Sun, L.J. Shin, S. Daewon, L. Youngil, Scripta Mater. **58**, 1010 (2008)
15. R.K. Raghava, K.P. Lee, A.I. Gopalan, J. Nanosci. Nanotechnol. **7**, 3117 (2007)
16. R.K. Raghava, K. Nakata, T. Ochiai, T. Murakami, D.A. Tryk, A. Fujishima, J. Nanosci. Nanotechnol. **11**, 3692 (2011)
17. R.K. Raghava, V.G. Gomes, M. Hassan, Mater. Res. Expr. **1**, 015012 (2014)
18. C. Murat, K.R. Reddy, A.M. Fernando, Chem. Eng. J. **309**, 151 (2017)
19. M. Hassan, E. Haque, K.R. Reddy, A.I. Minett, J. Chen, G.V. Gomes, Nanoscale **6**, 11988 (2014)
20. R.K. Raghava, K.P. Lee, A.I. Gopalan, Colloids Surf. A **320**, 49 (2008)
21. F. Jin, H. Zhang, X. Chen, X. Liu, Q. Chen, J. Sol-Gel Sci. Technol. **81**, 177 (2017)

22. J. Ma, Y. Cai, W. Wang, Q. Cui, M. Theingi, H. Zhang, Ceram. Int. **40**, 4963 (2014)
23. M. Eshraghi, P. Kameli, F. Khalili, M.H. Ehsani, H. Salamati, J. Rare Earths **32**, 965 (2014)
24. S. Das, T.K. Dey, Solid State Commun. **134**, 837 (2005)
25. C. Boudaya, L. Laroussi, E. Dhahri, J.C. Joubert, A. Cheikhrouhou, J. Phys. Condens. Mat. **10**, 7485 (1998)
26. G.H. Rao, J.R. Sun, K. Bärner, N. Hamad, J. Phys. Condens. Mat. **11**, 1523 (1999)
27. F.C. Fonseca, J.A. Souza, R.F. Jardim, R. Muccillo, E.N.S. Muccillo, D. Gouvea, M.H. Jung, A.H. Lacerda, J. Eur. Ceram. Soc. **24**, 1271 (2004)
28. X. Xu, J. Bullock, L.T. Schelhas, E.Z. Stutz, J.J. Fonseca, M. Hettick, V.L. Pool, K.F. Tai, M.F. Toney, X. Fang, A. Javey, L.H. Wong, J.W. Ager, Nano Lett. **16**, 1925 (2016)
29. R.K. Raghava, L.K. Pill, L. Youngil, G.A. Iyengar, Mater. Lett. **62**, 1815 (2008)
30. R.K. Raghava, S.B. Cheol, R.K. Sun, N. Jaegeun, L. Youngil, Synth. Met. **159**, 1934 (2009)
31. K.L. Yanapu, S.S. Samatham, D. Kumar, V. Ganesan, P.V. Reddy, Appl. Phys. A **122**, 1 (2016)
32. S. Hcini, S. Khadhraoui, S. Zemni, A. Triki, H. Rahmouni, M. Boudard, M. Oumezzine, J. Supercond. Novel Magn. **26**, 2181 (2013)
33. S.P. Schiffer, A.P. Ramirez W. Bao, S.W. Cheong, Phys. Rev. Lett. **75**, 3336 (1995)
34. E.S. Vlakhov, R.A. Chakalov, R.I. Chakalova, K.A. Nenkov, K. Dorr, A. Handstein, K.H. Muller, J. Appl. Phys. **83**, 2152 (1998)
35. H. Ahmed, S. Khan, W. Khan, R. Nongjai, I. Khan, J. Alloys Compd. **563**, 12 (2013)
36. T. Holstein, Ann. Phys. **8**, 343 (1959)
37. Y.K. Lakshmi, P.V. Reddy, J. Alloys Compd. **470**, 67 (2009)
38. D. Varshney, N. Dodiya, J. Theor. Appl. Phys. **9**, 45 (2014)
39. S.A. Ahmed, J. Magn. Magn. Mater. **340**, 131 (2013)
40. T. Nakajima, Y. Ueda, J. Alloys Compd. **383**, 135 (2014)
41. S.O. Manjunatha, A. Rao, V.P.S. Awana, G.S. Okram, J. Magn. Magn. Mater. **394**, 130 (2015)
42. S.O. Manjunatha, A. Rao, T.Y. Lin, C.M. Chang, Y.K. Kuo, J. Alloys Compd. **619**, 303 (2015)
43. S. Bhattacharya, S. Pal, R.K. Mukherjee, B.K. Chaudhuri, S. Neeleshwar, Y.Y. Chen, S. Mollah, H.D. Yang, J. Magn. Magn. Mater. **269**, 359 (2004)
44. S.T. Yazdi, P. Iranmanesh, J. Magn. Magn. Mater. **365**, 100 (2014)
45. T.D. Thanh, L.H. Nguyen, D.H. Manh, N.V. Chien, P.T. Phong, N.V. Khiem, L.V. Hong, N.X. Phuc, Phys. B **407**, 145 (2012)
46. F. Yonglai, Appl. Phys. Lett. **77**, 118 (2000)